THE ACTIVE ASTEROIDS

David Jewitt

Department of Earth and Space Sciences, UCLA, Los Angeles, CA 90095-1567, USA; jewitt@ucla.edu
Department of Physics and Astronomy, UCLA, Los Angeles, CA 90095-1567, USA

ABSTRACT

Some asteroids eject dust, unexpectedly producing transient, comet-like comae and tails. First ascribed to the sublimation of near-surface water ice, mass-losing asteroids (also called "main-belt comets") can in fact be driven by a surprising diversity of mechanisms. In this paper, we consider 11 dynamical asteroids losing mass, in nine of which the ejected material is spatially resolved. We address mechanisms for producing mass loss including rotational instability, impact ejection, electrostatic repulsion, radiation pressure sweeping, dehydration stresses, and thermal fracture, in addition to the sublimation of ice. In two objects (133P and 238P) the repetitive nature of the observed activity leaves ice sublimation as the only reasonable explanation, while in a third ((596) Scheila), a recent impact is the cause. Another impact may account for activity in P/2010 A2, but this tiny object can also be explained as having shed mass after reaching rotational instability. Mass loss from (3200) Phaethon is probably due to cracking or dehydration at extreme ($\sim$1000 K) perihelion temperatures, perhaps aided by radiation pressure sweeping. For the other bodies, the mass-loss mechanisms remain unidentified, pending the acquisition of more and better data. While the active asteroid sample size remains small, the evidence for an astonishing diversity of mass-loss processes in these bodies is clear.

Key words: comets: general – minor planets, asteroids: general

Online-only material: color figures

1. INTRODUCTION

The classification of small bodies in the inner solar system as either asteroids or comets has historically been attempted by different scientists using different techniques and employing different criteria. Observational astronomers classify small bodies having transient, unbound atmospheres (usually made visible by the scattering of sunlight from entrained micron-sized dust particles) as "comets." Bodies having instead a constant geometric cross section are called "asteroids." To planetary scientists, comets and asteroids are distinguished by their ice content or perhaps by their formation location. Comets are icy (because they formed beyond the "snow-line"), while asteroids are not (supposedly because they formed at higher mean temperatures inside it). Lastly, to dynamicists, comets and asteroids are broadly distinguished by a dynamical parameter, most usually the Tisserand parameter measured with respect to Jupiter (Kresak 1982; Kosai 1992). It is defined by

$$T_{\rm J} = \frac{a_{\rm J}}{a} + 2\left[(1-e^2)\frac{a}{a_{\rm J}}\right]^{1/2}\cos(i),\qquad(1)$$

where a, e, and i are the semimajor axis, eccentricity, and inclination of the orbit, respectively, while $a_{\rm J} = 5.2$ AU is the semimajor axis of the orbit of Jupiter. This parameter, which is conserved in the circular, restricted three-body problem, provides a measure of the close-approach speed to Jupiter. Jupiter itself has $T_{\rm J} = 3$. Main-belt asteroids have $a \leqslant a_{\rm J}$ and $T_{\rm J} > 3$, while dynamical comets have $T_{\rm J} < 3$.

The three systems of classification (observational, compositional, and dynamical) are independent but imperfect. For example, whether a coma or tail is detected on a given object depends strongly on the parameters of the observing system used. A puny telescope may not reveal a coma that is easily rendered visible by a more powerful one. There is neither an agreed quantitative ice fraction with which to divide comets from asteroids nor, more importantly, any reliable way to measure the ice fraction in a small body. The formation locations and dynamical histories of small bodies are rendered uncertain by hard-to-model non-gravitational forces from both electromagnetic radiation (the Yarkovsky effect) and mass loss itself (the rocket effect of Whipple 1950) and also by the chaotic nature of solar system dynamics. The Tisserand criterion is an imperfect classifier because it is based on an idealized representation of the solar system (e.g., Jupiter's orbit is not a circle, the gravity of other planets is not entirely negligible, and so on). Therefore, the utility of Equation (1) as a dynamical discriminant is limited for objects with $T_{\rm J}$ very close to 3. As an example, the quasi-Hilda comets at $a \sim 4.0$ AU have $T_{\rm J} \sim 2.9$–3.04 but are clearly interacting with Jupiter through the 3:2 mean-motion resonance (Toth 2006). Some recognized Jupiter family comets (e.g., 2P/Encke with $T_{\rm J} = 3.03$) also fall in this category (Fernández et al. 2002; Levison et al. 2006).

Given these and other imperfections, it is remarkable that, for a majority of objects, the observational, compositional, and dynamical definitions of asteroids and comets lie in close agreement. For the most part, objects classified as asteroids (comets) based on their orbits have the physical properties expected of asteroids (comets) as far as can be observed. Exceptions have given rise to a somewhat confusing and evolving system of nomenclature, used to describe small solar system bodies by a combination of their orbital properties and physical appearances. To clarify this, we show, in Figure 1, a two-parameter classification based on morphology, on the one hand, and the Tisserand parameter on the other. Traditional comets lose mass and have $T_{\rm J} < 3$. Those with $2 \leqslant T_{\rm J} < 3$ are called Jupiter family comets and are thought to originate in the Kuiper Belt. Comets with $T_{\rm J} < 2$ are long-period or Halley family comets, with a source in the Oort Cloud. Inactive counterparts to the Jupiter family comets are called, variously,
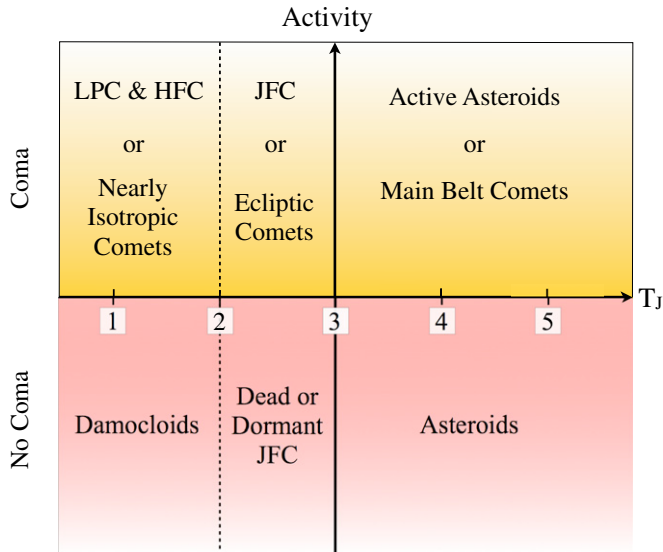
Figure 1. Empirical classification of small solar system bodies by (vertical axis) morphology and (horizontal axis) Tisserand dynamical parameter, T_J. In the figure, LPC = long-period comet, HFC = Halley family comet, and JFC = Jupiter family comet. The dynamical classification using Equation (1) assumes $a \leqslant a_J$.

(A color version of this figure is available in the online journal.)

extinct, dead, or dormant comets (Hartmann et al. 1987). They are presumably former comets in which past heating by the Sun has removed all near-surface ice, although buried ice might remain and these objects could, in principle, reactivate. Inactive counterparts to the long-period and Halley family comets are called Damocloids (Jewitt 2005). Again, these are likely objects in which near-surface ice has been lost.

In this paper, we focus attention on the sub-set of the small bodies that are dynamically asteroid-like ($a < a_J$, $T_J > 3$) but which lose mass, like comets. These were called "main-belt comets" by Hsieh & Jewitt (2006), but here we use the term "active asteroids," since some of the examples to be considered, while dynamically asteroid-like and showing comet-like properties, are not in the main belt. Numerical integrations show that these are not recently captured comets from the Kuiper Belt (Fernández et al. 2002; Levison et al. 2006). Scientific interest in these objects lies in the possibility that primordial water ice could have survived in asteroids despite early heating from embedded radioactive nuclei (Grimm & McSween 1989) and heating by the Sun. Even greater interest is added by the possibility that the outer asteroid belt may have supplied part of the volatile inventory of the Earth (Morbidelli et al. 2000). Additionally, active asteroids are a source of dust for the Zodiacal cloud, while unseen counterpart bodies may supply dust to the debris disks of other stars (e.g., Shannon & Wu 2011).

After briefly summarizing the current observational evidence concerning these active asteroids, we discuss the surprisingly varied mechanisms through which a body is capable of losing mass. A recent and complementary discussion focused on observational properties has been offered by Bertini (2011).

2. OBSERVATIONS OF ACTIVE ASTEROIDS

To date, 11 active (or mass-shedding) asteroids have been reported. The nine spatially resolved examples are shown for comparison in Figure 2, while their positions in the semimajor
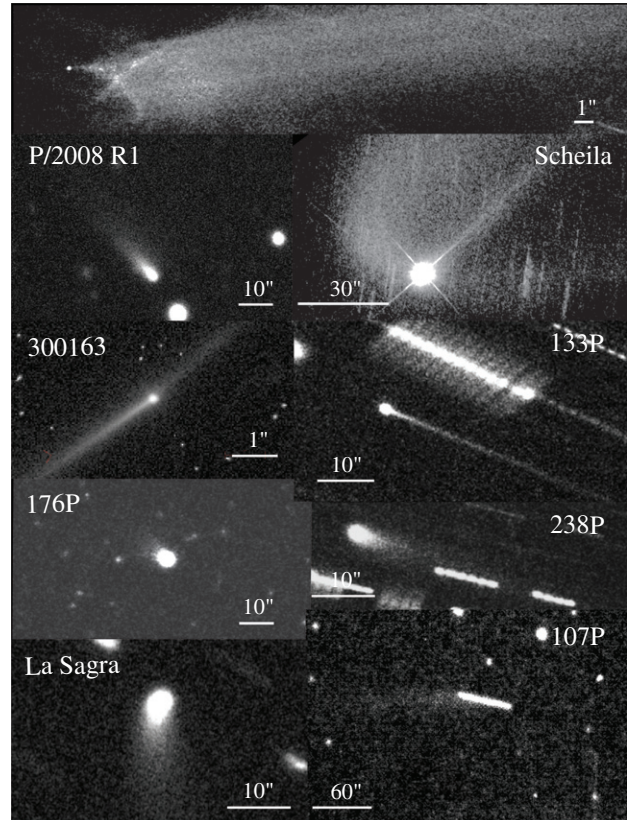

Figure 2. Images of nine spatially resolved active asteroids, with scale bars, in the order of decreasing Tisserand parameter, showing their comet-like appearances. Sources of the images are P/2010 A2 (Jewitt et al. 2010b), P/2008 R1 (Jewitt et al. 2009), (596) Scheila (Jewitt et al. 2011b), 300163 (D. Jewitt et al. 2012, in preparation), 133P (Hsieh et al. 2004), 176P (Hsieh & Jewitt 2006), 238P (Hsieh et al. 2009b), La Sagra (H. Hsieh 2011, private communication), and 107P (Fernández et al. 1997).

axis versus eccentricity plane are plotted in Figure 3. The comet-like morphologies and their orbital separation from the domain of the comets are obvious in these two figures. All 11 objects are located inside the 2:1 mean-motion resonance with Jupiter at 3.3 AU, and all but three lie below the Mars-crossing line (marked $q = Q^{\text{Mars}}$ in the figure). The orbital properties of these objects are summarized in Table 1, the physical properties in Table 2, and we review them briefly here, in order of decreasing T_J.

(3200) Phaethon: $T_J = 4.508$. This object is dynamically associated with the Geminid meteor stream (e.g., Williams & Wu 1993) and with several other small asteroids including 2005 UD (Ohtsuka et al. 2006; Jewitt & Hsieh 2006; Konoshita et al. 2007) and 1999 YC (Ohtsuka et al. 2008; Kasuga & Jewitt 2008). All these objects may be related to a precursor body that disintegrated $\sim 10^3$ yr ago (Ohtsuka et al. 2006). Evidence for modern-day mass loss comes from the observed brightening of Phaethon by a factor of two within a few hours of perihelion ($R = 0.14$ AU) in 2009 (Jewitt & Li 2010). This rapid brightening cannot be due to scattering from the ~ 5 km diameter nucleus alone and, instead, indicates transient mass loss with the ejection of $\sim 10^8 a_1$ kg of particles each a_1 mm in radius. With $a_1 = 1$ mm, this is only 10^{-4} of the Geminid stream mass, but it raises the possibility that the decay of Phaethon is a continuing process. The phenomenon has not been observed to repeat, but comparable observations when near perihelion are difficult to secure because of the small angular separation from the Sun.
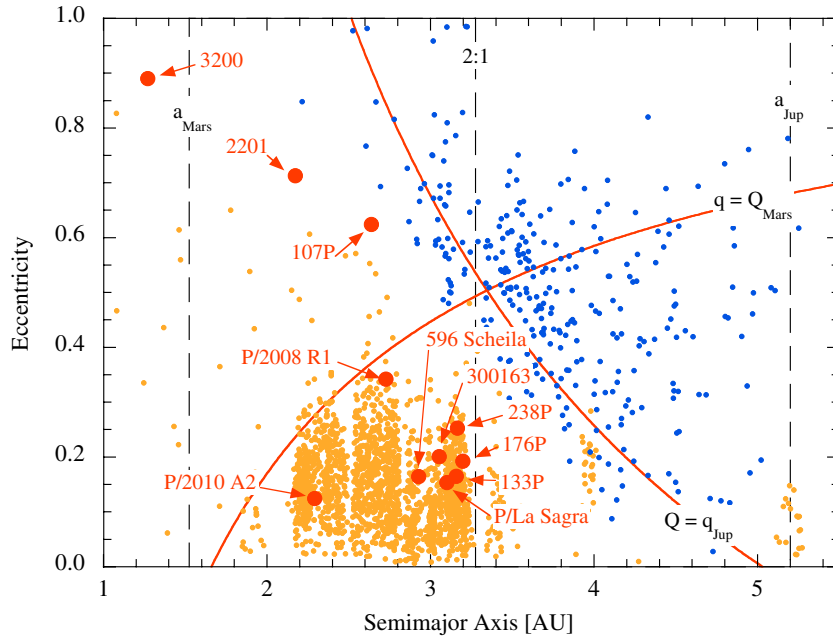
Figure 3. Distribution of the active objects (red circles) in the semimajor axis vs. orbital eccentricity plane. The corresponding distributions of asteroids (orange circles) and comets (blue circles) are shown for comparison. Objects above the diagonal arcs cross either the aphelion distance of Mars or the perihelion distance of Jupiter, as marked. The semimajor axes of the orbits of Mars and Jupiter are shown for reference, as is the location of the 2:1 mean-motion resonance with Jupiter.

(A color version of this figure is available in the online journal.)

Table 1
Summary of Orbital Properties

Name	T_J[a]	a[b]	e[c]	i[d]	q[e]	Q[f]
(3200) Phaethon	4.508	1.271	0.890	22.17	0.140	2.402
P/2010 A2	3.582	2.291	0.124	5.26	2.007	2.575
(2201) Oljato	3.299	2.172	0.713	2.52	0.623	3.721
P/2008 R1 (Garradd)	3.216	2.726	0.342	15.90	1.794	3.658
(596) Scheila	3.208	2.928	0.165	14.66	2.445	3.411
300163 (2006 VW139)	3.203	3.052	0.201	3.24	2.438	3.665
133P/Elst–Pizarro	3.184	3.157	0.165	1.39	2.636	3.678
176P/LINEAR (118401)	3.167	3.196	0.192	0.24	2.582	3.810
238P/Read	3.152	3.165	0.253	1.27	2.364	3.966
P/2010 R2 (La Sagra)	3.098	3.099	0.154	21.39	2.622	3.576
107P/Wilson–Harrington	3.083	2.638	0.624	2.79	0.993	4.284

Notes.
[a] Tisserand parameter with respect to Jupiter.
[b] Semimajor axis (AU).
[c] Orbital eccentricity.
[d] Orbital inclination.
[e] Perihelion distance (AU).
[f] Aphelion distance (AU).

P/2010 A2: $T_J = 3.582$. The object showed a distinctive morphology in which a leading, point-like nucleus about 120 m in diameter (Table 2) is followed by an extended tail (or trail) of dust in which are embedded ribbon-like structures (Jewitt et al. 2010b). The position angle of the tail and its variation with time are consistent with the action of radiation pressure on millimeter- to centimeter-sized dust particles, following impulsive ejection at very low speeds ($\sim$0.2 m s^{-1}) in 2009 February–March (Jewitt et al. 2010b; Snodgrass et al. 2010). (Note that an opposite conclusion was reached by Moreno et al. 2010 but based on limited data.) P/2010 A2 went unnoticed for its first $\sim$9 months largely because of its angular proximity to the Sun (Jewitt et al. 2011a). During this time, a large quantity of fast-moving particles are

presumed to have left the vicinity of the main nucleus. The mass of particles remaining in the tail at discovery is estimated to be in the range $(6$–$60) \times 10^7$ kg (Jewitt et al. 2010b; Moreno et al. 2010; Snodgrass et al. 2010).

(2201) Oljato: $T_J = 3.299$. Magnetometers on the *Pioneer Venus* spacecraft revealed multiple, symmetric disturbances in the solar wind magnetic field, clumped non-randomly in time (Russell et al. 1984). About 25% of these events are associated with planet-crossing asteroid (2201) Oljato, whose orbit lies interior to Venus' when near perihelion. Russell et al. suggested that the magnetic disturbances result from deceleration of the solar wind, perhaps caused by mass loading from ionized gases released by an unknown process from debris distributed along Oljato's orbit. A mass loading rate of only $\sim$5 kg s^{-1} is reportedly needed. However, a spectroscopic search for gas produced by Oljato itself proved negative (Chamberlin et al. 1996), with upper limits to the CN production rate near 10^{23} s^{-1}. With a standard H_2O/CN mixing ratio of 360, the corresponding limit to the mass production rate in water is $\leqslant$1.5 kg s^{-1}. Whatever the cause of the repetitive magnetic disturbances, they are not products of an inert asteroid and imply mass loss from Oljato. A dynamical simulation indicates that (2201) Oljato has negligible chance of being a captured Jupiter family comet (Bottke et al. 2002).

P/2008 R1: $T_J = 3.216$. This object was observed over a $\sim$45 day interval in 2008, when near $R = 2$ AU, as having the appearance of an active comet with a typically flared tail (Jewitt et al. 2009). The object intrinsically faded by a factor of about two over the above interval of observations. An upper limit to the nucleus radius of 0.7 km was set (red geometric albedo 0.05 assumed, see Table 2), later reduced to $r_n \leqslant$ 0.2 km by subsequent observations (H. Hsieh 2011, private communication). Spectral observations limited the production of the CN radical to $Q_{CN} \leqslant 1.4 \times 10^{23}$ s^{-1}, again corresponding to a water production rate $\leqslant$1.5 kg s^{-1} assuming $H_2O/CN = 360$. P/2008 R1 is located near the 8:3 mean-motion resonance

Table 2
Summary of Physical Properties

Name	D^a	$p_V{}^b$	P^c	$B - V^d$	dm/dt^e
(3200) Phaethon[1]	5–7	0.08–0.17	3.6	0.59 ± 0.01	N/A
P/2010 A2[2]	0.12	0.1^f	?	?	N/A
(2201) Oljato[3]	1.8	0.43 ± 0.03	?	?	5? (gas)
P/2008 R1 (Garradd)[4]	<0.4	0.04^f	?	0.63 ± 0.03	$\leqslant 1.5$ (gas), 0.01
(596) Scheila[5]	113 ± 2	0.038 ± 0.004	15.848	0.71 ± 0.03	$\leqslant 3$ (gas)
300163 (2006 VW139)[6]	3	0.04^f	?	?	?
133P/Elst–Pizarro[7]	3.8 ± 0.6	0.05 ± 0.02	3.471 ± 0.001	0.65 ± 0.03	<0.04 (gas), 0.01, 0.7-1.6
176P/LINEAR (118401)[8]	4.0 ± 0.4	0.06 ± 0.02	22.23 ± 0.01	0.63 ± 0.02	0.1
238P/Read[9]	0.8	0.05^f	?	0.63 ± 0.05	0.2
P/2010 R2 (La Sagra)[10]	1.4	0.04^f	?	?	4
107P/Wilson–Harrington[11]	3.5 ± 0.3	0.06 ± 0.01	7.15	?	$\leqslant 150$ (gas)

Notes.
[a] Effective diameter (km).
[b] Geometric albedo.
[c] Rotation period.
[d] Color index.
[e] Inferred mass-loss rate in kg s^{-1}. Unless otherwise stated, the estimates are based on continuum measurements and refer to dust. N/A means that no mass-loss rate can be specified because the loss is not in steady state.
[f] Value is assumed, not measured.

References. (1) Dundon 2005; (2) Jewitt et al. 2010b; (3) Tedesco et al. 2004; Russell et al. 1984; (4) Jewitt et al. 2009; (5) Tedesco et al. 2002; Warner 2006; (6) Hsieh et al. 2011a; (7) Hsieh et al. 2004, 2009a, 2011b; (8) Hsieh et al. 2012; Licandro et al. 2011; (9) Hsieh et al. 2011c; (10) Moreno et al. 2011a; Hsieh et al. 2012; (11) Veeder et al. 1984; Fernández et al. 1997; Licandro et al. 2009; Urakawa et al. 2011.

with Jupiter and is also affected by the ν_6 secular resonance. The dynamical lifetime in this orbit is short (20–30 Myr) compared with the age of the solar system, suggesting that P/2008 R1 was scattered into its present location from elsewhere in the asteroid belt.

(596) Scheila: $T_J = 3.208$. (596) Scheila, a 113 km diameter object with red geometric albedo ~ 0.04 (Table 2), developed a coma in late 2010. Over the course of a month, this coma expanded with a characteristic speed ~ 60 m s^{-1} and faded in response to the action of solar radiation pressure (Bodewits et al. 2011; Jewitt et al. 2011b; Moreno et al. 2011b), apparently without any continued replenishment of particles from the nucleus. The gas production from the nucleus was reportedly limited to $Q_{OH} \leqslant 10^{25}$ s^{-1} (Moreno et al. 2011b) to $Q_{OH} \leqslant 10^{26}$ s^{-1} (Howell & Lovell 2011), corresponding to water production rates $\leqslant 0.3$–3 kg s^{-1} (the meaning of these limits is unclear given the non-steady nature of the mass-loss event from Scheila). The mass of dust in micron-sized grains was 4×10^7 kg (Jewitt et al. 2011b), while more model-dependent attempts to account for mass in larger particles gave 6×10^8 kg (Bodewits et al. 2011) to 2×10^{10} kg (Moreno et al. 2011b). No ice was observed in the coma (Yang & Hsieh 2011).

300163 (2006 VW139): $T_J = 3.203$. Discovered in 2006 and first observed to be active on UT 2011 August 30 (Hsieh et al. 2011a), little is yet known about this object. With reported absolute magnitude $H = 16.6$ and an assumed albedo $p_V = 0.04$, appropriate to its outer belt location, the estimated diameter is ~ 3 km. Two thin tails, one near the projected orbit and another roughly antisolar, show that dust leaves the nucleus very slowly and point to mass loss over a protracted period. There is no reported evidence for gas or for repetitive mass loss, but new observations of this object are still being acquired at the time of writing.

133P/Elst–Pizarro: $T_J = 3.184$. The appearance is typically that of a point-like nucleus with a thin tail (or "trail") of $10\,\mu$m–sized dust following in the projected orbit. Order-of-

magnitude mass-loss rates in gas, inferred from spectroscopy (Licandro et al. 2011), and in dust, inferred from surface photometry of the tail (Hsieh et al. 2004), reach ~ 0.02 kg s^{-1}. The thin tail indicates that particles are ejected from the nucleus at speeds ~ 1.5 m s^{-1}, comparable to the escape speed from the 3.8 ± 0.6 km diameter nucleus.

176P: $T_J = 3.167$. A cometary appearance was detected for 176P/LINEAR over a single, month-long interval in 2005 (Hsieh et al. 2011b). During this time, the object showed a fan-shaped tail and was about 30% brighter than the bare nucleus, leading to an implied dust mass $\sim 10^5$ kg. The properties of the dust can be approximately matched by models in which the characteristic particle size is $10\,\mu$m, the ejection speed ~ 5 m s^{-1}, and the dust production rate ~ 0.07 kg s^{-1}, all similar to values inferred in 133P. The 4.0 ± 0.4 km diameter nucleus rotates with a period near 22.2 hr (Table 2).

238P/Read (= P/2005 U1): $T_J = 3.152$. Like P/2008 R1, the nucleus of 238P/Read is tiny, with a diameter ~ 0.8 km (Hsieh et al. 2012). It was observed to be in an active state in both 2005 and 2010, but not in between, with a coma dust mass of order 10^5 kg and a production rate estimated (from published photometry) near ~ 0.1 kg s^{-1}. Also like P/2008 R1, 238P/Read is dynamically short-lived, with a survival time of order 20 Myr (Haghighipour 2009).

P/2010 R2 (La Sagra): $T_J = 3.098$. The object was observed to be active from 2010 September to 2011 January, at $R = 2.6$–2.7 AU. Moreno et al. (2011a) inferred dust production at the peak rate of ~ 4 kg s^{-1}, with centimeter-sized particles ejected at about 0.1–0.2 m s^{-1}. A limit to the outgassing rate $Q_{CN} \leqslant 3 \times 10^{23}$ s^{-1} (corresponding to 3 kg s^{-1} in water) was placed spectroscopically (Hsieh et al. 2011c). Hsieh et al. (2011c) show (neglecting possible non-gravitational forces due to outgassing) that the orbit of P/2010 R2 is stable on timescales ~ 100 Myr and argue that this object was likely formed in situ.

107P/(1949 W1) Wilson–Harrington: $T_J = 3.083$. Fernández et al. (1997) analyzed two photographic plates taken on 1949

November 19, when at $R = 1.148$ AU. The object is trailed in both but, in the blue plate, shows a prominent diffuse tail about $2'$ in length. The red plate shows only a hint of this tail. The color ($B − R = −1$) is inconsistent with scattering from dust but suggests instead resonance fluorescent scattering from an ion tail. The position angle of the tail, being about $15°$ from radial to the Sun, is also more consistent with the expected direction of a plasma tail than with a dust tail. Curiously, 107P was re-observed on November 22 and 25 but then showed no trace of a tail (Cunningham 1950), and no comet-like activity has been reported since (Lowry & Weissman 2003; Ishiguro et al. 2011). Based on a statistical dynamical model, Bottke et al. (2002) concluded that there is a 4% chance that 107P is a captured Jupiter family comet.

3. MASS-LOSS MECHANISMS

We consider a variety of processes capable of launching dust from a small body. In each case, the number of unknown but relevant physical parameters prevents any exact treatment, but it remains instructive to consider the range of action of the mechanisms in the context of the asteroids.

3.1. Sublimation

Since Whipple (1950), sublimation has been explored in great detail as the driver of mass loss from the classical comets. It need not be re-described in detail here. Although simple in concept, detailed studies of comets show that sublimation is a remarkably complex process when factors such as the porosity of the surface, nucleus rotation, the conduction of heat into the interior, and the development of a refractory mantle are considered (Guilbert-Lepoutre & Jewitt 2011). One simplification possible for the present objects is the assumption that asteroids contain no amorphous ice, since temperatures in the asteroid belt are too high for it to escape crystallization. Accordingly, we address only the highly idealized case of sublimation from an exposed crystalline ice surface in thermal equilibrium with sunlight.

The sublimation mass flux per unit area, dm/dt (kg m^{-2} s^{-1}), from a patch of surface whose normal is inclined to the Sun-direction by angle θ is determined by solution of the energy balance equation

$$\frac{F_\odot (1 - A)}{R_{AU}^2} \cos(\theta) = \epsilon \sigma T^4 + L(T) \frac{dm(T)}{dt} + f_c. \quad (2)$$

Here, $F_\odot = 1360$ W m^{-2} is the solar constant, R_{AU} is the heliocentric distance in AU, A is the Bond albedo, $\epsilon \sim 0.9$ is the emissivity of the surface, $\sigma = 5.67 \times 10^{-8}$ W m^{-2} K^{-4} is the Stefan–Boltzmann constant, T is the equilibrium temperature, and $L(T)$ is the latent heat of sublimation. The temperature dependence of dm/dt may be estimated from thermodynamics and the Clausius–Clapeyron equation, or from direct measurement (Washburn 1926). The conduction term, f_c, requires knowledge of the thermophysical parameters and the spin vector of the nucleus and is small. We neglect it here.

The angle term, $\cos(\theta)$, depends on the nucleus rotation vector, changes with the position on the nucleus, and varies with time as the nucleus rotates. Therefore, the total mass-loss rate must be obtained by integrating Equation (2) over the surface and with respect to time. To avoid sinking in complexity, we here focus on two limiting cases for the surface temperature and resulting sublimation rate. The maximum temperature, T_{max}, is reached at the subsolar point on a non-rotating body, where
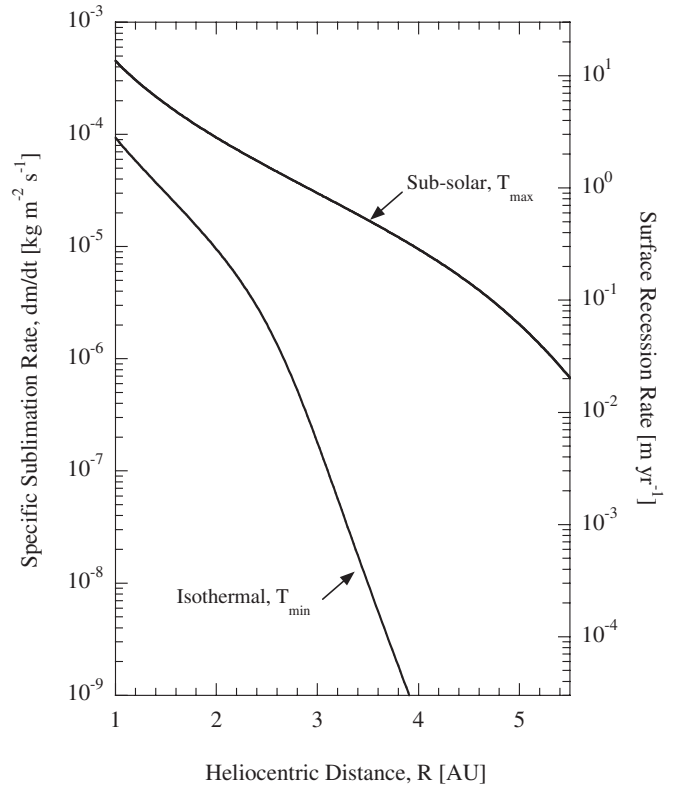

Figure 4. On the left, the equilibrium water ice sublimation rate (from Equation (2)) and, on the right, the surface recession rate (from Equation (3)), both as functions of the heliocentric distance. The curves are for albedo 0.05 and the maximum and minimum equilibrium temperatures, corresponding to the subsolar point on a non-rotating body and to an isothermal surface, respectively.

$\cos(\theta) = 1$. The minimum effective temperature, T_{min}, occurs when the surface is isothermal, corresponding to the largest possible radiating area. On a sphere, the average value of the angle term is $\overline{\cos(\theta)} = 1/4$. Accordingly, we estimate the minimum and maximum temperatures and specific sublimation rates from Equation (2) for $\overline{\cos(\theta)} = 1$ and $1/4$.

We considered both low ($A = 0.05$) and high ($A = 0.50$) ice albedos and calculated sublimation mass fluxes from Equation (2). Clean (high albedo) ice sublimates too slowly to drive activity at asteroid belt distances, and so we present only the dirty (low albedo) ice solutions for the sublimation rate as a function of distance, R, in Figure 4. The curves are convergent toward small R, because the sublimation term in Equation (2) is then dominant, but separate dramatically at larger R as the sublimation term drops exponentially, leaving all the energy for radiation.

Across the $2.0 \leqslant R \leqslant 3.3$ AU strip corresponding to the asteroid belt, sublimation rates from $\sim 10^{-4}$ kg m^{-2} s^{-1} (sublimation at T_{max}) to $< 10^{-8}$ kg m^{-2} s^{-1} (sublimation at T_{min}) are found. Mass-loss rates near 1 kg s^{-1} (Table 2) require sublimating areas from 10^4 m^2 (T_{max}) to 10^8 m^2 (T_{min}). Since the latter exceeds the entire surface area of (for example) 133P, we can exclude the isothermal (T_{min}) model as the activity driver. The main conclusion to be drawn from Figure 4 is that exposed water ice can sublimate across the full range of heliocentric distances occupied by the main belt provided it is dirty.

Two other quantities are directly calculable once dm/dt is known. First, the rate of recession of the sublimating surface is
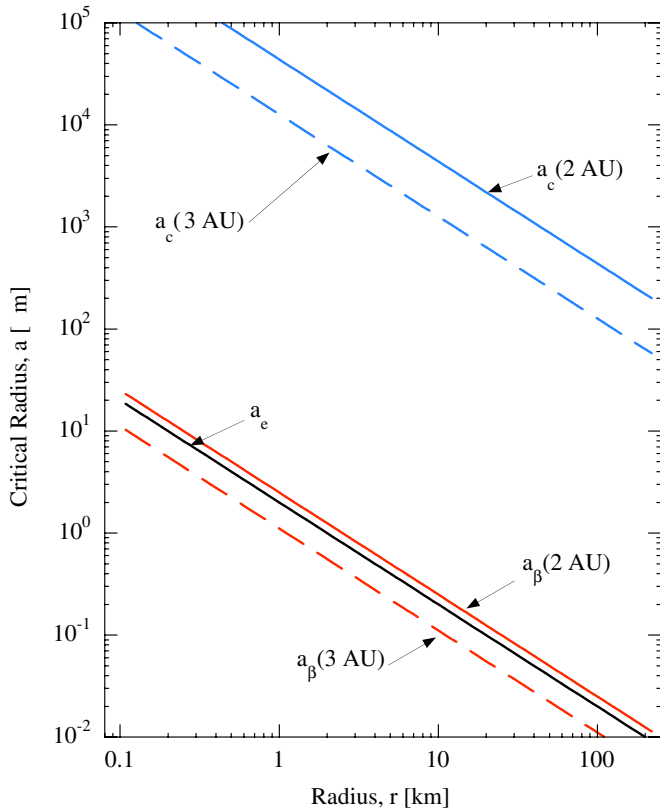
Figure 5. Critical dust grain radius for ejection by gas drag (a_c, computed from Equation (4)), for electrostatic ejection (a_e, Equation (13)), and for loss by radiation pressure sweeping (a_β, Equation (17)) as functions of nucleus radius. Solid and dashed curves for a_c and a_β refer to $R = 2$ AU and 3 AU, as marked.

(A color version of this figure is available in the online journal.)

given by

$$\frac{d\ell}{dt} = \frac{1}{\rho}\frac{dm}{dt} \qquad (3)$$

and indicated on the right-hand axis of Figure 4. With ice density $\rho = 1000$ kg m^{-3}, we find 350 μm yr$^{-1} \leqslant d\ell/dt \leqslant 3$ m yr^{-1} over the 2–4 AU distance range swept by the majority of active asteroids (see right-hand axis of the figure).

Second, the size of the largest ejectable particle is estimated by balancing the gas drag force with the gravity, assuming spherical particles and nucleus and neglecting all other forces. We take the densities of the ejected grains and of the bulk nucleus, in the absence of contrary evidence, to be equal. The resulting maximum particle radius, computed from

$$a_c = \frac{9}{16\pi}\frac{C_D V_{\text{th}}}{G\rho^2 r}\frac{dm}{dt}, \qquad (4)$$

is plotted in Figure 5 as a function of heliocentric distance for low-albedo, subsolar sublimation. In Equation (4), C_D is the dimensionless drag coefficient, here taken to be unity, and V_{th} is the gas speed at the nucleus surface, taken from Biver et al. (2002). The equation offers, at best, a crude estimate of the critical radius; the highly anisotropic outflow of gas from a real nucleus can strongly affect dust acceleration and dynamics relative to the simple isotropic case used here (e.g., Crifo et al. 2005). Still, it is obvious from Figure 5 that sublimation gas drag can easily remove small solid particles across the full range of distances swept by the main-belt asteroids. Grains larger than a_c remain bound to the asteroid and contribute to the development

of a refractory mantle, eventually leading to a stifling of the sublimation.

While exposed ice sublimates quickly, ice protected from direct illumination by a covering or mantle of refractory debris can survive nearly indefinitely. A meter-thick layer of regolith can suppress sublimation sufficiently to retain ice for Gyr timescales (Schorghofer 2008). Then, to initiate sublimation, this protective mantle must be removed, which could occur naturally through impact.

3.2. Impact Ejection

Collisions between asteroids occur at characteristic speeds of several km s^{-1} (Bottke et al. 1994) and are therefore highly erosive. Impact yields, defined as the ratio of the ejecta mass, m_e, to the projectile mass, M, are $m_e/M \gg 1$. Material ejected by impacts may explain observed activity in some asteroids. In this section we aim to obtain a relation between the impactor properties and the resulting brightening caused by ejected material.

In an impact, the bulk of the ejecta travel at the lowest speeds. For equal target and projectile densities, the mass of ejecta, m_e, traveling faster than a given speed, v, can be roughly expressed by a power law

$$m_e/M = A(v/U)^\alpha \qquad (5)$$

in which M and U are the impactor mass and speed and $A \sim 0.01$ is a constant (Housen & Holsapple 2011). The index α depends slightly on the properties of the target but is reasonably well approximated for a range of materials as $\alpha = -1.5$. Only ejecta traveling with $v \geqslant v_e$ can escape from an asteroid to produce an increase in the scattering cross section, while the rest must fall back to coat the surface around the impact site. With the escape velocity given by

$$v_e = \left(\frac{8\pi G\rho}{3}\right)^{1/2} r, \qquad (6)$$

it is clear that Equation (5) defines, for a given target density ρ and impact speed U, a relation between the impact yield and the radius, r, of the impacted asteroid.

A relation between m_e and the scattering cross section of the ejecta and hence the change in brightness caused by impact can be established. The size distribution of the ejecta from NASA's *Deep Impact* mission to comet 9P/Tempel 1 has been modeled as a power law (Kadono et al. 2010). Their Figure 4 gives a differential power-law size index $q = 3.7$ over the 1 μm $\leqslant a \leqslant$ 100 μm size range, while other investigators have found slightly steeper distributions (Lisse et al. 2006). Separately, the size distribution of the ejecta from P/2010 A2 has been modeled as a power law with $q = 3.3 \pm 0.2$ for 1 mm $\leqslant a \leqslant$ 10 mm (Jewitt et al. 2010b). A wider range of power laws (from $q = 3$ to as steep as $q = 6$) has been reported in small-scale, hypervelocity impact experiments (Takasawa et al. 2011). For the sake of the present discussion, we adopt $q = 3.5$ and find that the relation between the scattering cross section, C_e, and the mass of particles having radii in the range $a_{\min} \leqslant a \leqslant a_{\max}$ is

$$m_e = \frac{4}{3}\rho\bar{a}C_e, \qquad (7)$$

where $\bar{a} = (a_{\min}a_{\max})^{1/2}$. For example, with $a_{\min} = 0.1$ μm, $a_{\max} = 0.1$ m, $\bar{a} = 10^{-4}$ m, or 0.1 mm.

We combine Equations (5)–(7) to compute the ratio of the cross section of the ejecta to the cross section of the target

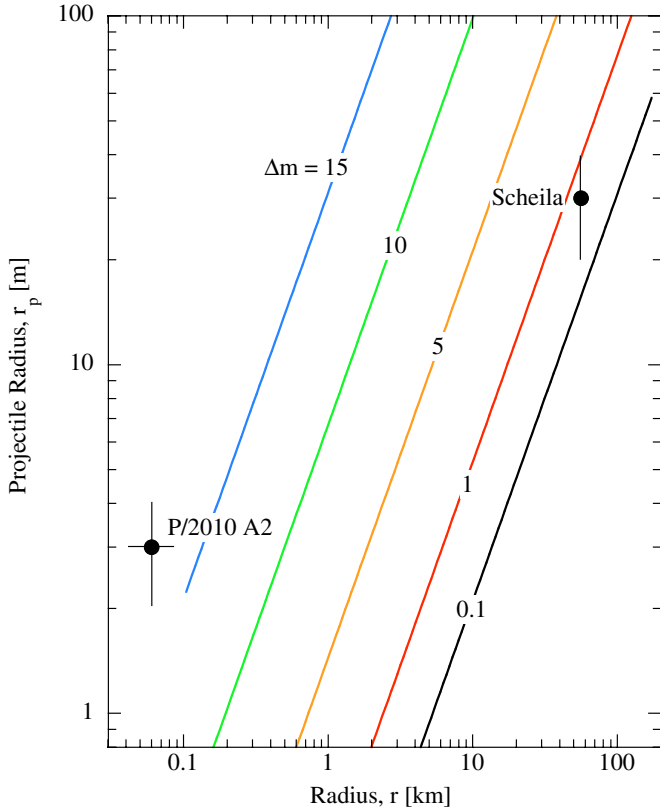**Figure 6.** Lines of constant brightening, in magnitudes, as a function of target and impactor radius. Impact velocity $U = 5000$ ms^{-1} and ejecta with a $q = 3.5$ differential size power law with particles in the 0.1 μm to 0.1 m size range were assumed. The radii of P/2010 A2 and (596) Scheila and their presumed impactors are shown, with error bars (the radius uncertainty for P/2010 A2 assumes a factor-of-two error in the assumed albedo).

(A color version of this figure is available in the online journal.)

asteroid

$$\frac{C_e}{\pi r^2} = \frac{A}{\bar{a} U^\alpha}\left(\frac{8\pi G\rho}{3}\right)^{\alpha/2} r_p^3 r^{\alpha-2}, \qquad (8)$$

where we have taken the projectile to be a sphere of the same density as the target and with a radius r_p. Substituting $A = 0.01$, $\bar{a} = 0.1$ mm, $U = 5$ km s^{-1}, $\rho = 2000$ kg m^{-3}, and $\alpha = -3/2$, we obtain

$$\frac{C_e}{\pi r^2} \sim 30\left(\frac{r_p}{1\,\text{m}}\right)^3\left(\frac{r}{1\,\text{km}}\right)^{-7/2}. \qquad (9)$$

A 1 m projectile impacting a 1 km target asteroid will produce ejecta with a cross section 30 times the geometric cross section of the asteroid.

Lines of constant brightening, computed from

$$\Delta m = 2.5 \log_{10}\left[1 + \frac{C_e}{\pi r^2}\right], \qquad (10)$$

are shown in Figure 6 as a function of asteroid and projectile radius. The curves are plotted only where the ejecta mass computed by Equation (5) is less than the target mass. The figure shows that, for example, the impact of a 1 m projectile into a 1 km asteroid would cause a brightening by $\Delta m \sim 3.5$ mag, while impact of the same projectile into a 10 km asteroid would cause a brightening of only a few $\times 0.01$ mag and would almost certainly escape detection. The published parameters of (596) Scheila and P/2010 A2, interpreted as impact ejecta, are also plotted in Figure 6. The location of Scheila overlaps the

$\Delta m = 1$ mag brightening line, consistent with observations. P/2010 A2 was discovered nearly a year after disruption. The magnitude of its initial brightening is thus unknown, but Figure 6 suggests that it was a dramatic $\Delta m \sim 15$. The curves in Figure 6 are uncertain, both because of the simplicity of the treatment and because of the many uncertainties in the impactor and dust grain parameters. For example, if U were larger by a factor of two, Equation (8) shows that the ejecta mass and cross section would be larger by a factor of ~ 2.8 and the ejecta would be brighter by ~ 1 mag. Nevertheless, Equation (8) and Figure 6 provide a useful first estimate of the observable effect of a given impact in the main belt. The figure leads naturally to the question of the impact rate in the main belt, which we discuss in Section 5.

While some ejecta can be launched from the impact site at speeds comparable to the impact speed (i.e., $v \sim U \sim 5$ km s^{-1}), most material travels much more slowly, following Equation (5). The slowest escaping material leaves the target at a speed comparable to the gravitational escape speed, thus setting a relation between the size of the target and the duration of the brightening caused by impact. For example, consider two target asteroids of size 100 m and 100 km, observed from 1 AU distance using a typical charge-coupled device camera with a field of view 5′ (corresponding to $\sim 10^5$ km half-width). Ejecta from the 100 km body will travel at ~ 100 m s^{-1} and cross the field of view in $\sim 10^6$ s (about 10 days). Ejecta from the 100 m body will travel at characteristic speed $v_e \sim 0.1$ m s^{-1} and take so long to cross the field ($\sim 10^9$ s) that radiation pressure and Keplerian shear will dominate the distribution of the dust. The persistence of impact-produced coma is thus a measure of the size of the target body.

3.3. Rotational Instability

The equatorial, centripetal acceleration on a strengthless rotating object of mass density ρ (kg m^{-3}) equals the gravitational acceleration at the critical rotational period, P_c, given by

$$P_c = k\left[\frac{3\pi}{G\rho}\right]^{1/2}. \qquad (11)$$

Here, k is a dimensionless constant dependent on the shape of the object. A sphere has $k = 1$. A prolate body with axes $a \geqslant b$ in rotation about its shortest dimension has $k \sim a/b$. Expressed in hours, Equation (11) may be written

$$P_c\,[\text{hr}] \sim 3.3k\left[\frac{1000}{\rho}\right]^{1/2}. \qquad (12)$$

For example, a sphere with $\rho = 2000$ kg m^{-3} has $P_c = 2.3$ hr while an elongated body with the same density and $a/b = 2$ has $P_c = 4.7$ hr, by Equation (12). Although Equation (12) shows that P_c is independent of the object size, numerous measurements of asteroids show that only objects smaller than ~ 0.1–0.3 km rotate with periods <2 hr (Pravec et al. 2002). The probable reason is that sub-kilometer asteroids have significant tensile strength and so can resist rotational disruption, while larger bodies are structurally weak and rotationally unstable when $P \leqslant P_c$. A weak (in tensile strength) aggregate or "rubble pile" structure could be produced by impact fracturing or, in the case of cometary nuclei, by the gentle settling together of icy planetesimals formed separately.

Given the evidence from the distribution of asteroid rotation rates, it is reasonable to conjecture that rotational instability might be a cause of observable mass loss in the main belt.

A number of torques are capable, in principle, of driving an asteroid into rotational instability. For example, collisions between asteroids lead to a random walk in angular momentum that can end in an unstable state. Anisotropic radiation of photons can lead to a net torque (the so-called YORP effect) that can do the same (Marzari et al. 2011; Jacobson & Scheeres 2011). An object losing mass through sublimation can, depending on the rate and angular dependence of the mass loss, experience a torque orders of magnitude larger than torques due to either collisions or YORP, quickly being driven toward rotational breakup (cf. Drahus et al. 2011). While, in principle, rotational instability can affect any asteroid regardless of its size, in practice the spin-up times vary inversely with radius and the objects most likely to experience rotational bursting are the smallest (exactly as observed in the near-Earth population). Could some active asteroids be rotationally disrupted objects?

3.4. Electrostatic Forces

The action of electrostatic forces in moving dust particles across a planetary surface is best established on the Moon. Images from the *Surveyor* lunar lander spacecraft showed an unexpected "horizon glow," caused by forward scattering from dust particles $\sim 10\,\mu$m in size located ~ 1 m above the surface (Rennilson & Criswell 1974). Later, the Lunar Ejecta and Meteorites (LEAM) dust detection experiment of Apollo 17 recorded the impact of low-velocity ($\leqslant 100\,$m s^{-1}) dust particles and showed particularly intense fluxes of such particles near local sunrise and sunset (Berg et al. 1976). The measured dust particle fluxes are ~ 7 orders of magnitude too large to be associated with churning of the surface by micrometeorite bombardment.

Instead, electrostatic levitation was suggested as the source of these particles. On the dayside, positive charging of the lunar surface occurs by ejection of electrons owing to the photoelectric effect from UV and X-ray solar photons. In the absence of a discharging current, the potential can rise to the energies of the most energetic photons (10^3 V, or more; cf. De & Criswell 1977), but, in practice, the measured dayside potential is about +10 V (Colwell et al. 2007). On the unilluminated side, or in shadows, the surface becomes negatively charged as a result of the greater flux of solar wind electrons (the solar wind is electrically neutral, but the low-mass electrons travel much faster than solar wind protons, leading to a net flux of electrons onto the surface). The typical energy of solar wind electrons is ~ 10 eV, leading to a negative potential of order 10 V. Near the terminator, the same processes lead to positive and negative charging of the surface, but on much smaller spatial scales corresponding to the scale of the local topography, leading to locally high electric field gradients. Near a shadow edge, the photoelectrons produced in sunlight can travel to and stick in unilluminated regions, causing local electric field gradients estimated at $E \sim 10$ to 100 V m^{-1} (Colwell et al. 2007; Farrell et al. 2007). The positive, sunlit surface attracts a cloud of electrons, effectively neutralizing the gradient on length scales $\ell \gtrsim 1$ m.

The electrostatic processes that move dust particles on the Moon presumably operate also on the asteroids. The charging time on the Moon is $\sim 10^2$–10^3 s (de & Criswell 1977); photoelectron charging currents will be nine times weaker at 3 AU and the charging times will be nine times longer, but the potentials attained, for a given dielectric constant, will remain the same. The principal difference in the asteroid belt is that, whereas levitated lunar dust is retained by the gravity of the Moon, dust ejection speeds on small bodies can exceed

the escape velocity, v_e. Therefore, electrostatic processes are potentially capable of leading to mass loss from asteroids.

The charge on a spherical grain of radius a is related to the potential on the grain, V, by $q = 4\pi\epsilon_0 V a$, where $\epsilon_0 = 8.854 \times 10^{-12}$ F m^{-1} is the permittivity of free space. The force on a charged particle exposed to an electric field E (V m^{-1}) is just $F_e = qE$. As our criterion for dust ejection, we demand $v > V_e$, where v is the grain speed achieved by accelerating across the shielding distance ℓ and V_e is the gravitational escape speed at the surface. Assuming that the grain and the asteroid are spherical, of radius a and r, respectively, and that both have density ρ, this criterion gives the critical grain size for electrostatic ejection as

$$a_e = \left(\frac{18\epsilon_0 V E \ell}{4\pi G \rho^2 r^2} \right)^{1/2}. \tag{13}$$

Substituting the lunar values, $V = 10$ V, $\ell = 1$ m, $E = 10$–100 V m^{-1}, and using $\rho = 2000$ kg m^{-3} as the canonical asteroid density, Equation (13) gives $a_e = 1.5$–$5\,\mu$m for an $r = 1$ km asteroid (cf. Figure 5). These sizes are somewhat smaller than the $\sim 10\,\mu$m sized particles inferred from observations of some active asteroids (e.g., 133P; Hsieh et al. 2004), but, given the many uncertainties in both the model and the interpretation of observations, perhaps the differences are acceptable. In contrast, Equation (13) shows that on the Moon ($r = 1600$ km), only nanometer-sized grains can be ejected, meaning that the process is irrelevant there. Even for asteroid (596) Scheila ($r = 56$ km and $a_e = 0.04$–$0.1\,\mu$m), any electrostatically ejected particles would be smaller than a wavelength and inefficient optical scatterers. Figure 5 shows that $a_e \sim 10^{-4} a_c$ for a given asteroid radius. We conclude that electrostatic ejection of particles large enough to scatter optical photons is a plausible mass-loss mechanism only for smaller asteroids.

There are major uncertainties concerning electrostatic effects on the Moon, especially regarding the tendency for small particles to stick to each other and to surfaces, through the action of Van der Waals and other contact forces. These uncertainties are magnified in importance on the asteroids because, unless the forces of cohesion can be overcome, electrostatic levitation and ejection will be impossible (Hartzell & Scheeres 2011). Unfortunately, ignorance of grain cohesion limits our ability to know whether electrostatic ejection is important on the asteroids, although flat, pond-like structures on Eros have been interpreted this way (Hughes et al. 2008). Sonnett et al. (2011) report that $\sim 5\%$ of main-belt asteroids show ultra-faint comae that cannot be detected individually but which are collectively significant. If these comae are real, electrostatic ejection of sub-micron grains might offer a plausible source mechanism that is approximately independent of distance from the Sun.

3.5. Thermal Fracture

Thermal fracture can occur when the stress associated with a change in the temperature of a material exceeds the tensile strength of the material. The thermal stress is $S \sim \alpha Y \delta T$, where α (K^{-1}) is the thermal expansivity, Y (N m^{-2}) is the Young's modulus, and δT (K) is the responsible temperature change. The expansivities of common rocks are $\alpha \sim 10^{-5}$ K^{-1} (Lauriello 1974; Richter & Simmons 1974). Young's moduli $Y = (10$–$100) \times 10^9$ N m^{-2} are typical for rock (Pariseau 2006, p. 474). If converted into kinetic energy with efficiency η, thermal strain energy can generate fractured material with

speeds (Jewitt & Li 2010)

$$v \sim \alpha \delta T \sqrt{\frac{\eta Y}{\rho}}. \qquad (14)$$

Substituting $\eta = 1$ gives an upper bound to the ejection speeds of fracture fragments as $v \sim 20 \, \mathrm{m \, s^{-1}}$, for fracture at $\delta T = 1000 \, \mathrm{K}$. This is sufficient to launch particles above the gravitational escape speed from asteroids up to radius $r \sim 20$ km. Thus, thermal fracture is a potential source of small particles and an agent capable of ejecting these particles from asteroids, but only those approaching the Sun very closely.

3.6. Thermal Dehydration

Some carbonaceous chondrite classes (probable fragments of outer-belt asteroids) contain 10%–20% water by weight, bound into hydrated minerals (Jarosewich 1990). If it could be liberated, this bound water might drive observable mass loss by entraining small grains in the gas flow produced as the water escapes into space.

Laboratory experiments show that thermal dehydration of hydrous phyllosilicates of planetary relevance (e.g., serpentine, brucite, muscovite, talc) is characterized by activation energies in the range 325–400 kJ mol^{-1} (Bose & Ganguly 1994). Thermal dehydration is accompanied by a net volume change that can crack the dehydrating material and provide a source of small particles. However, the above activation energies correspond to temperatures ($\sim$1000 K) much higher than normally found in the asteroid belt. For this reason, thermal dehydration is unlikely to play a role in a majority of the active asteroids since they have perihelia $\geqslant$2 AU and temperatures too low to trigger dehydration.

3.7. Shock Dehydration

Dehydration can be caused by shock pressure waves in impacts. For example, shock dehydration of brucite (Mg(OH)$_2$) begins near 12 GPa and is complete by 56 GPa (50% of the trapped water is lost at pressures 17 GPa; Duffy et al. 1991). Pressures this high are confined to a region comparable in size to the projectile diameter, so that the volume of shock-dehydrated target material is small compared with the volume of the resulting impact crater. Nevertheless, water released by impact could sustain mass loss from an asteroid for a timescale longer than that on which the impact ejecta dissipates. For example, a 10 m radius projectile would dehydrate $\sim$10^7 kg of target. With a water fraction of 10%, some 10^6 kg of water could potentially leak from the impact site, enough to sustain a dusty flow at 0.1 kg s^{-1} for $\sim$100 days. While shock dehydration must be considered, at best, a process of secondary importance, it does raise the prospect that gaseous products detected following an impact might, in the future, be misinterpreted as evidence for sublimating ice.

3.8. Radiation Pressure Sweeping

Dust particles can be swept from the surface of an asteroid through the action of radiation pressure. To see this, we consider a grain located just above the surface and compare the gravitational acceleration toward the nucleus with the acceleration in the anti-sunward direction caused by radiation pressure, the latter expressed as $\beta g_\odot$, where $g_\odot$ is the gravitational acceleration to the Sun. A dust particle can be swept away by radiation pressure if

$$\beta \frac{GM_\odot}{R^2} > \frac{4}{3}\pi G \rho r \qquad (15)$$

in which we have assumed that the nucleus is at heliocentric distance R and is spherical, of density ρ, radius r, and non-rotating. Also, G is the gravitational constant and $M_\odot$ is the mass of the Sun. The dimensionless quantity β depends on the grain shape, composition, and porosity but is principally a function of particle size, a. As a useful first approximation, we take $\beta \sim 1/a_\mu$, where a_μ is the grain radius expressed in microns (Bohren & Huffman 1983). Then, the condition for a grain to be lost to radiation pressure becomes

$$a_\beta < \frac{3 \, M_\odot}{4\pi \rho r R^2}. \qquad (16)$$

Substituting $\rho = 2000 \, \mathrm{kg \, m^{-3}}$ and expressing the nucleus radius in km and the heliocentric distance in AU, we find the critical radius for grain loss to be

$$a_\beta = 10 \left(\frac{1 \, \mathrm{km}}{r}\right) \left(\frac{1 \, \mathrm{AU}}{R}\right)^2. \qquad (17)$$

Equation (17) (also plotted in Figure 5) shows that, for example, a 1 km radius object at $R = 3$ AU would lose dust grains smaller than about $a \sim 1 \, \mu$m. Optically active particles ($a \geqslant 0.1 \, \mu$m) can be swept away throughout the asteroid belt provided their parent bodies are smaller than about 10 km. Larger particles can be lost if the nucleus is rotating and has an aspherical shape.

The above considerations are simplistic in that they take no account of the direction of the radiation pressure acceleration relative to the nucleus. Grains released on the dayside, for instance, will be pushed back into the nucleus by radiation pressure from above. On the other hand, grains released near the terminator will feel a net force in a direction determined by the vector sum of the local gravitational acceleration and radiation pressure acceleration. These grains have the potential to escape. The principal limitation to efficacy of radiation pressure sweeping is, as with electrostatic launch, set by contact forces that hold small particles to the asteroid surface. If these forces can be overcome, then radiation pressure sweeping can play a role across the asteroid belt for 10 km–sized asteroids and smaller.

4. MECHANISMS FOR INDIVIDUAL OBJECTS

4.1. 133P and 238P

The key observational property of these objects is that the activity is recurrent (Hsieh et al. 2004, 2010), qualitatively consistent with sublimation in the same way that mass loss from the classical comets is modulated by the varying insolation around the orbit. Other mechanisms in Section 3 either are inconsistent with recurrent mass loss (impact, rotational instability) or can be reconciled with it only in the most contrived way. With equilibrium sublimation rates $\lesssim$(3–5) $\times$ 10^{-5} kg m^{-2} s^{-1} at $R = 2.6$–3.0 AU (Figure 4), the most stringent production rates $\lesssim$0.01 kg s^{-1} (Table 2) imply mass loss from areas of exposed ice $\lesssim$200–300 m^2, corresponding to circles of radius $\sim$10 m (Hsieh et al. 2004).

The eccentricities of 133P and 238P are small (0.165 and 0.253, respectively), and over the range of heliocentric distances swept, the expected sublimation mass flux varies by less than an order of magnitude (upper curve in Figure 4). This is a problem
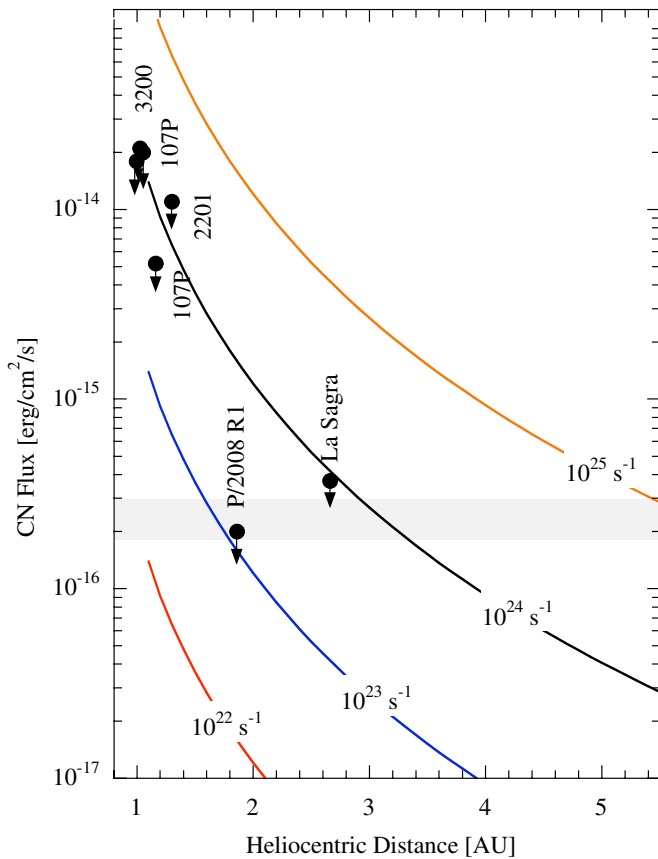
Figure 7. Heliocentric distance dependence of the CN band flux for CN production rates $Q_{CN} = 10^{22}$, 10^{23}, 10^{24}, and 10^{25} s^{-1}. The horizontal gray band shows the typical band sensitivity achievable using Keck in about an hour. Published limits to the CN flux are presented as black circles.

(A color version of this figure is available in the online journal.)

The fluxes in the figure were evaluated for opposition (i.e., $\Delta = R - 1$) and assume the Haser model and a spectroscopic slit $1'' \times 5''$. The Swings effect (in which the resonance fluorescence cross section is affected by the heliocentric velocity through the Doppler effect) amounts to less than a factor of two and has been neglected for simplicity. Plotted on the figure are published limits to the CN band flux in active asteroids. State-of-the-art measurements, indicated by the horizontal gray band in the figure, reach CN fluxes $\sim(2$–$3) \times 10^{-16}$ erg cm^{-2} s^{-1}, corresponding to $Q_{CN} \sim 10^{23}$ s^{-1} at $R = 2$ AU, but by $R = 3$ AU, the limits barely reach $Q_{CN} \sim 10^{24}$ s^{-1}, showing how difficult is the spectroscopic detection of gas at larger distances. The steep distance dependence is made worse by the rapidly declining sublimation rates from 2 AU to 3 AU (Figure 4). For the most favorable (high temperature) case in that figure (albedo 0.05) the sublimation rate drops by a factor of four from 2 AU to 3 AU. For these reasons, spectroscopic detection of gas at main-belt distances is challenging even in many classical comets, where sublimation is the undoubted driver of the observed activity. Insofar as spectroscopic emission detections of gas in active asteroids are concerned, absence of evidence is not evidence of absence.

4.2. (596) Scheila

The brightening of Scheila was sudden, the scattering cross section declined smoothly with time, and the morphology evolved in a way consistent with the expansion of an impulsively ejected coma under the action of radiation pressure (Bodewits et al. 2011; Jewitt et al. 2011b; Moreno et al. 2011b; Hsieh et al. 2012; Ishiguro et al. 2011). All these signatures are consistent with impact production but are difficult or impossible to reconcile with the other mechanisms of Section 3. Scheila is also alone among the active asteroids, so far, in being very large (113 km diameter). It presents a substantial cross section for impact, but the resulting strong gravity precludes the action of electrostatic ejection, while the slow rotation eliminates any possibility of rotational instability. Sublimation of water ice can eject small grains from Scheila, but the short coma fading time is difficult to understand given the sublimation rates in Figure 4.

The outburst brightness was ~ 1 mag brighter than the bare asteroid (Larson 2010; Jewitt et al. 2011b). Figure 6 is consistent with the conclusion that the projectile was between 35 m and 60 m in diameter (Jewitt et al. 2011b; Ishiguro et al. 2011; cf. Bodewits et al. 2011).

4.3. P/2010 A2

Impact may account for the dust tail of P/2010 A2, but the interpretation in this case is non-unique. This body is comparatively tiny (only 120 m in diameter versus 113 km for Scheila), with a tail mass suggesting collision with a projectile only a few meters in size (Jewitt et al. 2010b; Snodgrass et al. 2010). A key observational difference is that, whereas (596) Scheila faded on a timescale of one month, the tail of P/2010 A2 remained prominent ~ 15 months after formation, despite the addition of no new dust (Jewitt et al. 2010b, 2011b). This difference in fading timescales arises because the slowest particles to escape from a body leave the target with a speed comparable to the gravitational escape speed. For P/2010 A2 this is ~ 0.1 m s^{-1}, allowing large, slow grains to persist for >1 yr after impact, while, for Scheila, particles ejected at less than the 60 or 70 m s^{-1} escape speed simply fell back on the surface (Jewitt et al. 2011b; Ishiguro et al. 2011). Furthermore, most

because a 10-fold reduction in activity at aphelion relative to perihelion would still produce detectable dust, whereas none is observed. Instead, mass loss might be confined to a window near perihelion because of a shadowing effect of local topography on the nucleus, perhaps caused by recession of the sublimating surface, forming a pit (Equation (3)). The surface recession rate at $R = 2.6$–3.0 AU is $(3$–$5) \times 10^{-8}$ m s^{-1}, so that a sublimation pit meters deep should develop in only a few orbits. However, that the ice must still be close to the physical surface is shown by the appearance of comae near and soon after perihelion. Ice more than a few centimeters deep would be thermally decoupled from the deposition of heat on the surface.

The evidence for ice sublimation, although self-consistent, remains indirect. Detection of gaseous products of sublimation would provide definitive evidence for the role of sublimation in active asteroids. Just as in the classical comets, practical concerns render the daughter species (molecular fragments) optically more visible than the parent molecules sublimated from the ice. The most prominent band in the optical spectra of comets is due to the trace species CN, itself a product of dissociation of the parent molecule HCN. As noted in Section 2, several attempts to detect CN $\lambda 3889$ in active asteroids have been reported, typically resulting in limits to the total gas production rate 0.1–1 kg s^{-1}, about two to three orders of magnitude smaller than found in bright comets near 1 AU.

To set this on a quantitative basis, we show in Figure 7 the expected CN band flux as a function of R for several outgassing rates, as marked, computed as described in Jewitt et al. (2009).

Table 3
Summary of Mechanisms

Name	Sublimation	Impact	Electrostatics	Rotation	Thermal
(3200) Phaethon	×	?	?	?	✓
P/2010 A2	×	✓	×	✓	×
(2201) Oljato	?	?	?	?	×
P/2008 R1 (Garradd)	?	?	?	?	×
(596) Scheila	×	✓	×	×	×
300163 (2006 VW139)	?	?	?	?	×
133P/Elst–Pizarro	✓	×	?	?	×
176P/LINEAR (118401)	?	?	?	×	×
238P/Read	✓	×	×	?	×
P/2010 R2 (La Sagra)	?	?	?	?	×
107P/Wilson–Harrington	?	?	?	×	×

Notes. ✓: evidence exists consistent with the process; ×: evidence exists inconsistent with the process; ?: insufficient evidence exists.

grains traveling fast enough to be ejected were also small enough to be deflected by solar radiation pressure, providing another mechanism to quickly clear the coma. There are no direct measurements of the total, early-time brightening, only a limit $\Delta m < 19$ (Jewitt et al. 2011b). However, the model suggests that if the P/2010 A2 were hit by a 2 m–sized projectile, the brightening would be $\Delta m \sim 15$ (Figure 6), which is consistent with the empirical constraint. Extreme brightening caused by impact has been suggested as an explanation of "guest stars" recorded in ancient Chinese records (Reach 1992).

Rotational instability offers another explanation for mass loss from P/2010 A2 (Jewitt et al. 2010b). The small diameter of the primary body (120 m) corresponds to a short spin-up timescale under the action of YORP. In fact, for sub-kilometer main-belt objects the YORP spin-up timescale is less than the timescale for collisional disruption (Marzari et al. 2011; Jacobson & Scheeres 2011). While the rotation period of the primary body in P/2010 A2 is unknown, it would not be surprising to find that it had exceeded the centripetal limit. Unfortunately, there are few published predictions for the detailed appearance of a rotationally disrupted body (Richardson et al. 2005).

4.4. (3200) Phaethon

Object (3200) Phaethon is distinguished from the other active asteroids by its small perihelion, $q = 0.14$ AU, allowing it to reach extreme subsolar temperatures ($\sim$1000 K). These are sufficient to trigger thermal fracture and to dehydrate water-bearing minerals, if they are present (Jewitt & Li 2010). It has been suggested that Phaethon was recently scattered inward from a Pallas-like orbit ($a = 2.771$ AU, $e = 0.281$, $i = 33°$; de León et al. 2010), where a large proportion of the asteroids are volatile-rich B and C types. If Phaethon originated in the vicinity (or as part) of Pallas, then finding hydrated minerals would not be surprising, since Pallas itself contains hydrated minerals. The small asteroids associated dynamically with Phaethon (1999 YC and 2005 UD) should have similar compositions, but they have not been observed close to perihelion and have shown no evidence for mass loss.

In addition to the creation of dust and fragments by thermal fracture and dehydration shrinkage, we conjecture that the escape of particles produced by these thermal mechanisms is facilitated by radiation pressure sweeping. This is especially important in (3200) Phaethon near perihelion relative to other asteroids. According to Equation (17), particles up to $300\,\mu$m in diameter can be swept from its surface when at $q = 0.14$ AU.

Particles produced by thermal fracture or dehydration cracking, or lifted from the surface by electrostatic repulsion, would be rapidly swept away from it by radiation pressure (Jewitt & Li 2010).

4.5. Other Objects

The mechanisms behind the mass loss in other active asteroids remain less clear. Activity in 176P can be interpreted in terms of a sublimation model that is able to fit the observed coma morphology (Hsieh et al. 2010). Models involving impulsive ejection (e.g., by impact) reportedly provide less good fits to the imaging data, but, given the many unknown parameters in the models (e.g., the relation between dust particle size, scattering efficiency, and speed), the identification of sublimation in 176P cannot be regarded as definitive. The same must be said for observations of P/2008 R1, where sublimation can fit the data (Jewitt et al. 2009) but where an impact origin may also apply. We also regard the nature of activity in P/2008 R1 as unknown. The coma isophotes of P/La Sagra are consistent with dust emission over an extended period (Moreno et al. 2011b), as is integrated light photometry (after correction for the unmeasured phase function of the comet; cf. Hsieh et al. 2012). Again, isophote models involve the assumption of numerous, unknown parameters and provide solutions that are non-unique. This is especially true for objects viewed at small angles to their orbital planes, as are most of the active asteroids. Clear evidence of the weakness of models is the fact that Moreno et al. (2010), using limited data, were able to fit the isophotes of P/2010 A2 with a model in which particles were released over an eight-month period, inconsistent with the finding of an impulsive origin based on more and better imaging data (Jewitt et al. 2010b; Snodgrass et al. 2010). With this as a cautionary reminder, we regard the evidence concerning activity in 176P, P/2008 R1, P/La Sagra, and 300163 as insufficient to diagnose the cause. Evidence concerning 107P and (2201) Oljato is even more fragmentary, and the cause of their activity is also unknown.

The results of this and the previous section are summarized for convenience in Table 3 and shown schematically in Figure 8. The figure shows the plane of object radius, r, versus heliocentric distance, R, with the regions of action of the different physical processes considered in Section 3 marked as color fields. The 11 reported active asteroids are plotted at the heliocentric distances at which activity was observed. The figure shows that, for example, (596) Scheila lies in a region of the r versus R plane in which only impact and sublimation are capable of
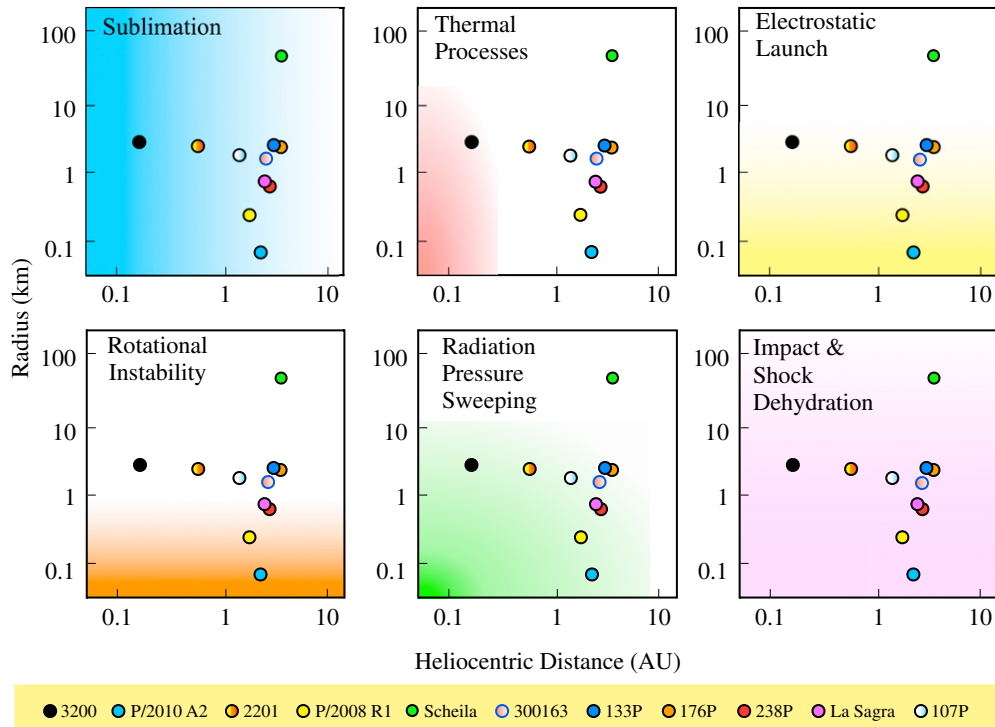
Figure 8. Schematic diagrams of object radius vs. heliocentric distance, with color fields marking the regions of action of the physical processes discussed in the text. The color-coded circles denote the radii and distances at which mass loss has been reported in 11 active asteroids, identified in the key at the bottom.

(A color version of this figure is available in the online journal.)

ejecting particles. (As described above, detailed studies of the morphology and time dependence of the coma of Scheila show that impact is the true explanation.) Conversely, a majority of the active asteroids lie in regions of the r versus R plane where many processes are potentially important. For example, in 238P, sublimation, electrostatic ejection, rotational instability, radiation pressure, and impact process are all potentially active. Only through detailed physical investigation is it possible to discriminate between these possibilities (in favor of sublimation, in the case of 238P, based principally on the repetition of the observed mass loss). For many active asteroids, the physical observations needed to discriminate among mechanisms do not exist.

5. DISCUSSION

Collisions are implicated in active asteroids both directly, as in the case of (596) Scheila and, perhaps, P/2010 A2, and indirectly as a trigger for activity (for example, to expose buried ice), as in 133P and 238P. Here, we briefly examine the expected rate of collision between asteroids.

The typical collision probability per unit area in the asteroid belt is $P_c \sim 3 \times 10^{-18}$ km^{-2} yr^{-1}, with variations by a factor of several reflecting a collisional environment that varies with location in the belt (Bottke et al. 1994). The interval between impacts onto an asteroid of radius r is

$$\tau_c = \frac{1}{\pi r^2 P_c N_p(\geqslant r_p)}, \qquad (18)$$

where $N(\geqslant r_p)$ is the number of impactors larger than r_p. Estimates of the size distribution of the asteroids are many and varied, with significant uncertainties resulting from the unmeasured albedos of most asteroids, as well as from severe

observational bias effects (Jedicke et al. 2002). The uncertainties are particularly acute for sub-kilometer asteroids because such objects are faint and remain largely unobserved. For radii $r > 1$ km, the best-fitting differential power-law index is about -2, albeit with significant, size-dependent deviations from this value. For radii $r \leqslant 1$ km, perhaps the best constraints on the distribution come from the impact crater size distribution on asteroid Gaspra. There, craters from 0.4 km to 1.5 km in diameter (caused by projectiles perhaps 10–20 times smaller) are distributed as a power law with a differential size index -3.7 ± 0.5 (Belton et al. 1992; note that Chapman et al. (1996) report that *fresh* craters on Gaspra follow an even steeper distribution, with differential power-law index -4.3 ± 0.3). We assume that the total main-belt population is $\sim 1.4 \times 10^6$ asteroids with diameters >1 km. Combining these results and integrating over the size distribution, we take the number of projectiles with radius $\geqslant r_p$ as

$$N_p(\geqslant r_p) = 2.6 \times 10^{13} \left(\frac{r_p}{1\,\mathrm{m}}\right)^{-2.7}, \qquad (19)$$

where r_p is expressed in meters. Equations (18) and (19) together give

$$\tau_c = 4200 \left(\frac{r_p}{1\,\mathrm{m}}\right)^{2.7} \left(\frac{r}{1\,\mathrm{km}}\right)^{-2} (\mathrm{yr}), \qquad (20)$$

with r in km. Lines of constant collision time from Equation (20) are plotted in Figure 9. Impacted asteroid (596) Scheila is marked on Figure 9 with an error bar indicating different estimates of the projectile radius from Jewitt et al. (2011b, $a \sim 17$ m) and Ishiguro et al. (2011, $a \sim 40$ m), respectively. The corresponding collision times are 3×10^3 yr $\leqslant \tau_c \leqslant 3 \times 10^4$ yr. Given that there are ~ 250 known asteroids as large as or larger than (596) Scheila, the mean interval between similar events is $\sim (10-100)$ yr, statistically consistent with the detection of
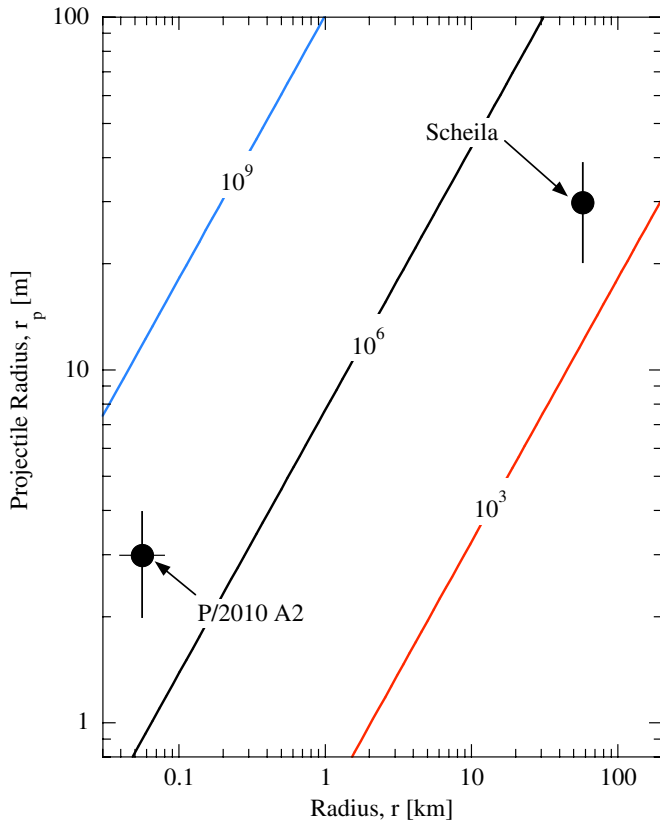
Figure 9. Collision time, in years, as a function of target asteroid radius, for projectiles having radii 1–100 m, as marked. Lines of constant collision time were computed from Equation (20). Impact candidates P/2010 A2 and (596) Scheila are shown with error bars reflecting independent estimates of the projectile radii, as discussed in the text.

(A color version of this figure is available in the online journal.)

Scheila within the first decade of efficient, nearly real-time sky monitoring.

Disrupted asteroid P/2010 A2 (interpreted as a ~60 m radius object impacted by a projectile of characteristic size 2–4 m; Jewitt et al. 2010b) is also marked in Figure 9, indicating a collision time $\tau_c \sim (7–50) \times 10^6$ yr. With $N(\geqslant 60) \sim 4 \times 10^8$ (Equation (19)), the expected rate of similar events is ~8–60 yr^{-1}. Jewitt et al. (2011b) estimated the detection probability of P/2010 A2 clones as $\lesssim 6\%$, so that of 8–60 similar events per year we would currently detect only ~0.5–4. This is still higher than the actual rate of detection, counted as one object in perhaps a decade of efficient, nearly real-time sky monitoring by LINEAR and other survey telescopes. The high rate could simply indicate the extreme uncertainty in using Equation (19) to estimate the number of meter-sized projectiles. For example, the equation gives $N_p(\geqslant 5) = 3 \times 10^{11}$, while published estimates of this number range from ~$10^{9.5}$ to ~10^{12} (Davis et al. 2002), indicating a large uncertainty in τ_c at small projectile sizes. Or it could indicate that activity in P/2010 A2 is caused by another process, possibly YORP spin-up, as remarked in Section 4.3. Further progress in understanding the impact rate in the asteroid belt hinges strongly on better measurements of the sub-kilometer size distribution.

Future wide-area sky surveys may help elucidate the mechanisms operating to cause asteroidal mass loss. For example, we expect the spatial distribution of collisionally produced or triggered objects to be correlated with the regions of the asteroid belt in which the collision probability per unit time is highest.

Unfortunately, the published surveys for active asteroids so far either are biased (Hsieh 2009) or, if unbiased, detected no objects and so provide insufficient information (Gilbert & Wiegert 2009, 2010; Sonnett et al. 2011). All but one of the known active asteroids were discovered serendipitously by a variety of surveys and methods, most too poorly quantified in terms of reported areal coverage and limiting magnitude to be used to interpret the spatial distribution. This dismal situation deserves to be soon corrected by well-characterized, all-sky surveys having sensitivity sufficient to discover substantial numbers of active asteroids.

6. SUMMARY

The number of mechanisms capable of producing mass loss from asteroids rivals the number of asteroids showing evidence for mass loss. No single mechanism can account for the varied examples of activity observed, but preferred explanations can be suggested for particular objects.

1. Sublimation of crystalline ice is effective to the outer edge of the asteroid belt and in asteroids up to a few 100 km in size. Observational evidence for the sublimation of water ice is strongest in the two repeatedly active objects 133P/Elst–Pizarro and 238P/Read.
2. Activity in (596) Scheila is unambiguously caused by the impact of a decameter-sized projectile, as indicated by the photometric and morphological evolution of this body.
3. Rotational instability is likewise broadly operable, but it is the sub-kilometer asteroids that are most likely to be driven toward instability by YORP effects. The 120 m diameter P/2010 A2, if it is not also an impact relic, could be a rotationally disrupted body.
4. Thermal fracture and dehydration cracking are expected to supply dust particles only on asteroids that are very close to the Sun ($\ll 1$ AU) and smaller than about 20 km. Radiation pressure sweeping can remove grains from 10 km asteroids up to 3 AU but is more effective at smaller distances. All these processes may operate in small perihelion object (3200) Phaethon.
5. Ejection of optically active grains (i.e., $> 0.1\,\mu$m) by the electrostatic mechanism is possible for asteroids up to about 10–20 km in radius with an efficiency that is independent of heliocentric distance. No clear examples of this process have been identified.
6. The causes of mass loss from the other active asteroids cannot be reliably determined given the limited available data (see Table 3).

REFERENCES

Belton, M. J. S., Veverka, J., Thomas, P., et al. 1992, Science, 257, 1647
Berg, O. E., Wolf, H., & Rhee, J. 1976, in Proc. Colloq. on Interplanetary Dust and Zodiacal Light, Vol. 48, ed. H. Elsasser & H. Fechtig (Heidelberg: Springer), 233
Bertini, I. 2011, Planet. Space Sci., 59, 365
Biver, N., Bockelée-Morvan, D., Colom, P., et al. 2002, Earth Moon Planets, 90, 5
Bodewits, D., Kelley, M. S., Li, J.-Y., et al. 2011, ApJ, 733, L3
Bohren, C. F., & Huffman, D. R. 1983, Absorption and Scattering of Light by Small Particles (New York: Wiley)
Bose, K., & Ganguly, J. 1994, Am. Mineral., 79, 692

Bottke, W. F., Morbidelli, A., Jedicke, R., et al. 2002, Icarus, 156, 399
Bottke, W. F., Nolan, M. C., Greenberg, R., & Kolvoord, R. A. 1994, Icarus, 107, 255
Chamberlin, A. B., McFadden, L.-A., Schulz, R., Schleicher, D. G., & Bus, S. J. 1996, Icarus, 119, 173
Chapman, C. R., Veverka, J., Belton, M. J. S., Neukum, G., & Morrison, D. 1996, Icarus, 120, 231
Colwell, J. E., Batiste, S., Horányi, M., Robertson, S., & Sture, S. 2007, Rev. Geophys., 45, 2006
Crifo, J.-F., Loukianov, G. A., Rodionov, A. V., & Zakharov, V. V. 2005, Icarus, 176, 192
Cunningham, L. 1950, IAU Circ., 1250, 3
Davis, D. R., Durda, D. D., Marzari, F., Campo Bagatin, A., & Gil-Hutton, R. 2002, in Asteroids III, ed. W. F. Bottke, Jr., A. Cellino, P. Paolicchi, & R. P. Binzel (Tucson, AZ: Univ. Arizona Press), 545
de, B. R., & Criswell, D. R. 1977, J. Geophys. Res., 82, 999
de León, J., Campins, H., Tsiganis, K., Morbidelli, A., & Licandro, J. 2010, A&A, 513, A26
Drahus, M., Jewitt, D., Guilbert-Lepoutre, A., et al. 2011, ApJ, 734, L4
Duffy, T. S., Ahrens, T. J., & Lange, M. A. 1991, J. Geophys. Res., 961, 14319
Dundon, L. 2005, MS thesis, Univ. Hawaii
Farrell, W. M., Stubbs, T. J., Vondrak, R. R., Delory, G. T., & Halekas, J. S. 2007, Geophys. Res. Lett., 34, 14201
Fernández, J. A., Gallardo, T., & Brunini, A. 2002, Icarus, 159, 358
Fernández, Y. R., McFadden, L. A., Lisse, C. M., Helin, E. F., & Chamberlin, A. B. 1997, Icarus, 128, 114
Gilbert, A. M., & Wiegert, P. A. 2009, Icarus, 201, 714
Gilbert, A. M., & Wiegert, P. A. 2010, Icarus, 210, 998
Grimm, R. E., & McSween, H. Y., Jr. 1989, Icarus, 82, 244
Guilbert-Lepoutre, A., & Jewitt, D. 2011, ApJ, 743, 31
Haghighipour, N. 2009, Meteorit. Planet. Sci., 44, 1863
Hartmann, W. K., Tholen, D. J., & Cruikshank, D. P. 1987, Icarus, 69, 33
Hartzell, C. M., & Scheeres, D. J. 2011, Planet. Space Sci., 59, 1758
Housen, K. R., & Holsapple, K. A. 2011, Icarus, 211, 856
Howell, E. S., & Lovell, A. J. 2011, IAU Circ., 9191, 2
Hsieh, H., Denneau, L., & Wainscoat, R. 2011a, IAU, CBET, 2920
Hsieh, H. H. 2009, A&A, 505, 1297
Hsieh, H. H., Ishiguro, M., Lacerda, P., & Jewitt, D. 2011b, AJ, 142, 29
Hsieh, H. H., & Jewitt, D. 2006, Science, 312, 561
Hsieh, H. H., Jewitt, D., & Fernández, Y. R. 2009a, ApJ, 694, L111
Hsieh, H. H., Jewitt, D., & Ishiguro, M. 2009b, AJ, 137, 157
Hsieh, H. H., Jewitt, D., Lacerda, P., Lowry, S. C., & Snodgrass, C. 2010, MNRAS, 403, 363
Hsieh, H. H., Jewitt, D. C., & Fernández, Y. R. 2004, AJ, 127, 2997
Hsieh, H. H., Meech, K. J., & Pittichová, J. 2011c, ApJ, 736, L18
Hsieh, H. H., Yang, B., & Haghighipour, N. 2012, ApJ, 744, 9
Hughes, A. L. H., Colwell, J. E., & Dewolfe, A. W. 2008, Icarus, 195, 630
Ishiguro, M., Ham, J.-B., Tholen, D. J., et al. 2011, ApJ, 726, 101
Jacobson, S. A., & Scheeres, D. J. 2011, Icarus, 214, 161
Jarosewich, E. 1990, Meteoritics, 25, 323
Jedicke, R., Larsen, J., & Spahr, T. 2002, in Asteroids III, ed. W. F. Bottke, Jr., A. Cellino, P. Paolicchi, & R. P. Binzel (Tucson, AZ: Univ. Arizona Press), 71
Jewitt, D. 2005, AJ, 129, 530
Jewitt, D., Annis, J., & Soares-Santos, M. 2010a, IAU Circ., 9109, 3
Jewitt, D., & Hsieh, H. 2006, AJ, 132, 1624
Jewitt, D., & Li, J. 2010, AJ, 140, 1519
Jewitt, D., Stuart, J. S., & Li, J. 2011a, AJ, 142, 28
Jewitt, D., Weaver, H., Agarwal, J., Mutchler, M., & Drahus, M. 2010b, Nature, 467, 817
Jewitt, D., Weaver, H., Mutchler, M., Larson, S., & Agarwal, J. 2011b, ApJ, 733, L4
Jewitt, D., Yang, B., & Haghighipour, N. 2009, AJ, 137, 4313
Kadono, T., Sugita, S., Ootsubo, T., et al. 2010, Earth, Planets Space, 62, 13
Kasuga, T., & Jewitt, D. 2008, AJ, 136, 881
Konoshita, D., Ohtsuka, K., Sekiguchi, T., et al. 2007, A&A, 466, 1153
Kosai, H. 1992, Celest. Mech. Dyn. Astron., 54, 237
Kresak, L. 1982, Bull. Astron. Inst. Czech., 33, 104
Larson, S. M. 2010, IAU Circ., 9188, 1
Lauriello, P. 1974, Int. J. Rock Mech. Min. Sci. Geomech. Abstr., 11, 75
Levison, H. F., Terrell, D., Wiegert, P. A., Dones, L., & Duncan, M. J. 2006, Icarus, 182, 161
Licandro, J., Campins, H., Kelley, M., et al. 2009, A&A, 507, 1667
Licandro, J., Campins, H., Kelley, M., et al. 2011, A&A, 525, A34
Lisse, C. M., VanCleve, J., Adams, A. C., et al. 2006, Science, 313, 635
Lowry, S. C., & Weissman, P. R. 2003, Icarus, 164, 492
Marzari, F., Rossi, A., & Scheeres, D. J. 2011, Icarus, 214, 622
Morbidelli, A., Chambers, J., Lunine, J. I., et al. 2000, Meteorit. Planet. Sci., 35, 1309
Moreno, F., Lara, L. M., Licandro, J., et al. 2011a, ApJ, 738, L16
Moreno, F., Licandro, J., Ortiz, J. L., et al. 2011b, ApJ, 738, 130
Moreno, F., Licandro, J., Tozzi, G.-P., et al. 2010, ApJ, 718, L132
Ohtsuka, K., Arakida, H., Ito, T., Yoshikawa, M., & Asher, D. J. 2008, Meteorit. Planet. Sci. Suppl., 43, 5055
Ohtsuka, K., Sekiguchi, T., Kinoshita, D., et al. 2006, A&A, 450, L25
Pariseau, W. G. 2006, Design Analysis in Rock Mechanics (London: Taylor and Francis)
Pravec, P., Harris, A. W., & Michalowski, T. 2002, in Asteroids III, ed. W. F. Bottke, Jr., A. Cellino, P. Paolicchi, & R. P. Binzel (Tucson, AZ: Univ. Arizona Press), 113
Reach, W. 1992, Meteoritics, 27, 353
Rennilson, J. J., & Criswell, D. R. 1974, Moon, 10, 121
Richardson, D. C., Elankumaran, P., & Sanderson, R. E. 2005, Icarus, 173, 349
Richter, D., & Simmons, G. 1974, Int. J. Rock Mech. Min. Sci. Geomech. Abstr., 11, 403
Russell, C. T., Aroian, R., Arghavani, M., & Nock, K. 1984, Science, 226, 43
Schorghofer, N. 2008, ApJ, 682, 697
Shannon, A., & Wu, Y. 2011, ApJ, 739, 36
Snodgrass, C., Tubiana, C., Vincent, J.-B., et al. 2010, Nature, 467, 814
Sonnett, S., Kleyna, J., Jedicke, R., & Masiero, J. 2011, Icarus, 215, 534
Takasawa, S., Nakamura, A. M., Kadono, T., et al. 2011, ApJ, 733, L39
Tedesco, E. F., Noah, P. V., Noah, M., & Price, S. D. 2002, AJ, 123, 1056
Tedesco, E. F., Noah, P. V., Noah, M., & Price, S. D. 2004, IRAS Minor Planet Survey, IRAS-A-FPA-3-RDR-IMPS-V6.0, NASA Planetary Data System, http://tinyurl.com/769yag2
Toth, I. 2006, A&A, 448, 1191
Urakawa, J., Okumura, S. I., Nishiyama, K., et al. 2011, Icarus, 215, 17
Veeder, G. J., Kowal, C., & Matson, D. L. 1984, Lunar Planet. Inst. Sci. Conf. Abstracts, 15, 878
Warner, B. D. 2006, Minor Planet Bull., 33, 58
Washburn, E. 1926, International Critical Tables of Numerical Data, Physics, Chemistry and Technology, Vol. 3 (New York: McGraw-Hill)
Whipple, F. L. 1950, ApJ, 111, 375
Williams, I. P., & Wu, Z. 1993, MNRAS, 262, 231
Yang, B., & Hsieh, H. 2011, ApJ, 737, L39